Reducing the RTM backscattering noise via wavefield decomposition in the $f - k$ domain

Kristian D.T. Bautista
Department of Physics, The University of Alberta

GEOPH 526 – Signal Processing in Geophysics
Fall term, 2019

ABSTRACT

Reverse Time Migration (RTM) is a powerful migration technique that uses the full two-way wave equation as an engine to produce high-quality seismic images of the Earth's subsurface reflectivity. In the presence of complicated geological settings, however, RTM images severely suffer from low-frequency, high-amplitude noise, which is mainly a consequence of the correlation of backscattered waves along the wave path at non-reflecting points. For both source and receiver wavefields, the two-way propagator generates backscattered events at sharp boundaries or in regions with high-contrast velocity interfaces. Thus, one approach to remove the backscattering noise consists of separating each wavefield into its one-way components and then correlating components that travel in opposite directions. In this report, I implement a 2D Fourier-based wavefield decomposition strategy that conveniently separates the downgoing and upgoing components of the source and receiver wavefields using a filtering technique in the $f-k$ domain. Then, I apply a decomposed imaging condition that preserves causality and allows for better, more refined imaging. Numerical tests applied on two 2D synthetic data sets demonstrate that this method effectively improves the quality of the RTM image by eliminating the backscattered energy from conventional RTM. Finally, I also identify some of the disadvantages of this approach, mostly related to its computational efficiency.

INTRODUCTION

Seismic migration is a subsurface imaging method that aims to position seismic data into their true temporal or spatial reflector positions. In order to meet the current energy demand, the oil and gas industry has been directing hydrocarbon exploration to deeper and more challenging geological prospects, which naturally requires the development of more sophisticated and robust migration algorithms. Despite its high computational cost, pre-stack reverse time migration (RTM) (Baysal et al., 1983) is now considered as the preferred technique for imaging complex geological settings, thanks to the advances in high-performance computing. Since it is the only migration algorithm that employs the two-way wave equation in the downward continuation process, RTM can overcome the limitations of ray-based and one-way wave equation-based migration techniques, given a sufficiently accurate velocity model. The superiority of this method in providing better subsurface images stems from the fact that the two-way extrapolation is a more faithful approximation of the wave propagation phenomena in the Earth (Etgen et al., 2009).

Despite all of its advantages, a characteristic high-amplitude, low-frequency migration noise that is uncorrelated with the geology usually pollutes the raw image output from RTM. These artifacts are not a consequence of the approximations that RTM makes, but rather caused by undesired features in the fundamental imaging principle that correlates the source and receiver wavefields (Leveille et al., 2011). For instance, if the velocity model has singularities such as the sharp top of a salt body, then the source wavefield is not consistently downgoing because the two-way modeling engine simulates scattered waves in all directions. When the backscattered waves in the source wavefield are cross-correlated with the upgoing components of the receiver wavefield, intense backscattered "artifacts" are formed along the wave path at non-reflecting points due to the constructive interference of such components traveling in the same direction. A completely parallel analysis can be done for the cross-correlation between the downgoing backscattered components of the receiver wavefield and the downgoing components of the source wavefield. This phenomenon breaks the fundamental imaging principle that strictly assumes destructive interference between source and receiver wavefields except at reflecting points in the subsurface (Claerbout, 1985).

Even though the backscattered energy contains crucial information about the long-wavelength section of the Earth model and it is useful for velocity building techniques, it is typically conceived as noise in seismic imaging because it masks the reflectors (Díaz and Sava, 2012). A straightforward post-imaging approach for removing the low-frequency artifacts in the migration image is the implementation of a high-pass spatial filter such as a Laplacian operator, as proposed by Zhang and Sun (2009). Despite its high computational efficiency, this operator does not preserve the global relative amplitude information, which is crucial for reservoir analysis. It is also an isotropic operator (i.e., dip independent), therefore it still cannot provide satisfactory results under many situations (Jing and Anderson, 2019). Another post-imaging alternative involves a signal/noise separation by least-squares filtering, where the signal is defined as the reflectivity, and the noise is the backscattered energy (Guitton et al., 2007). On the other hand, Fletcher et al. (2006) proposed modifying the wave equation with a directional damping term to suppress internal backscattered reflections. Yoon and Marfurt (2006) utilized the Poynting vector to obtain the wave propagation directions and then discarding large-angle wavefields to prevent the migration artifacts. However, this method is not stable when the wavefield derivatives are zero, thus, it is not capable of handling complicated velocity models (Jin et al., 2014).

It is also possible to apply wavefield decomposition as a noise removal strategy before forming the RTM image. This method is based on the decomposition of source and receiver wavefields in their one-way components along a certain direction to correlate the appropriate combinations of some of these decomposed wavefields. Liu et al. (2011) performed a wavefield decomposition based on the Hilbert transform to separate wavefields into up-going and down-going wave components. Other wavefield decomposition strategies involve implementations in the curvelet domain (Wang et al., 2013), and the wavelet domain (Paniagua-Castrillón and Quintero-Montoya, 2018). In this work, I implement a unidirectional wavefield decomposition strategy based on the 2D Fourier transform, using the symmetry properties of the $f-k$ domain and cut-off filters. This methodology was first applied to vertical seismic profiles (VSP) (Hu and McMechan, 1987), and used recently by Wang et al. (2016) to break down the full-waveform inversion gradient. It allows for an explicit separation into upgoing and downgoing components, which are used later to form RTM images with a decomposed imaging condition that preserves the benefits of the two-way propagation. This report is organized into four parts. The first one is this introduction, which is followed by a brief review of RTM theory and a description of the wavefield decomposition technique in the $f-k$ domain. The third part presents the numerical experiments used to validate my algorithm. Finally, the conclusions are presented.

METHODOLOGY

Reverse time migration

The concept of RTM is based on the time-space domain wavefield extrapolation and an imaging condition (Baysal et al., 1983; Whitmore, 1983). The implementation of this method is rather straightforward, and can be synthesized in three steps. First, the algorithm propagates the seismic source wavelet, $f(t)$, forward in time over a previously estimated background velocity model, $v(\vec{x})$, to get the source wavefield, $s(\vec{x},t)$, using the “full” two-way acoustic wave equation:

$$\left(\frac{1}{v^2(\vec{x})}\frac{\partial^2}{\partial t^2}-\nabla^2\right)s\left(\vec{x},t\right)=f\left(t\right)\delta\left(\vec{x}-\vec{x}_s\right), \tag{1}$$

where $\vec{x}=(x,y,z)$ is the subsurface imaging location, $\vec{x}_s$ denotes the source position, and ∇^2 is the Laplacian operator. Likewise, the recorded field data, $d(\vec{x}_r;\vec{x}_s;t)$, are backward propagated in time from the receiver locations, $\vec{x}_r$, to generate the receiver wavefield, $r(\vec{x},t)$:

$$\left(\frac{1}{v^2(\vec{x})}\frac{\partial^2}{\partial t^2}-\nabla^2\right)r\left(\vec{x},t\right)=d\left(\vec{x}_r;\vec{x}_s;t\right). \tag{2}$$

The last step consists of applying the conventional zero-lag cross-correlation imaging condition between the source and receiver wavefields to produce the RTM image, m_{mig}. For a single shot, this operation can be expressed as:

$$m_{\text{mig}}(\vec{x})=\int_0^{\mathrm{T_{max}}}s(\vec{x},t)r(\vec{x},t)\,dt. \tag{3}$$

The final stacked RTM section is formed by adding one more integral to Equation 3, accounting for all the shots in the seismic survey. Although this imaging condition provides the correct kinematics for a reflection in which incident and reflected wavefields are coincident in space and time, it generates the backscattered noise described in the previous section, as well as other migration artifacts (i.e., it is amplitude-deficient).

Since the two-way wave equation is used in the RTM extrapolation process, the source and receiver wavefields have both up-going and down-going components. Therefore, Equation 3 can be rewritten as:

$$m_{\text{mig}}(\vec{x})=\int_0^{\mathrm{T_{max}}}\left(s_dr_u+s_ur_d+s_dr_d+s_ur_u\right)dt, \tag{4}$$

where space and time variables have been suppressed for simplicity, and the sub-indexes d and u denote the down-going and up-going propagation directions defined with respect to time increases. The first two pairs, s_dr_u and s_ur_d, causally cross-correlate incident and reflected waves only at reflecting points. The last two pairs, s_ur_u and s_dr_d, have the same propagation directions and are acausally and constructively cross-correlated along the entire wave path when the integration over time is applied. As explained in the previous section, the low-frequency noise is associated with these terms. Therefore, we can neglect them from Equation 3 to form a decomposed imaging condition that is conceptually free of backscattering noise:

$$m_{\mathrm{mig}}(\vec{x}) = \int_0^{\mathrm{T_{max}}} (s_d r_u \ + s_u r_d)\, dt \tag{5}$$

The next section presents the strategy adopted in this study to deblend the wavefields into vertical components, allowing the implementation of the decomposed imaging condition.

Wavefield decomposition in the $f - k$ domain

To illustrate how the wavefield decomposition in the $f-k$ domain works, we take the source wavefield as an example, and define its down-going component in terms of the 2D inverse Fourier transform:

$$s_d(z,t) = \frac{1}{4\pi^2} \int_{-\infty}^{+\infty} \int_{-\infty}^{+\infty} \hat{S}(k_z,\omega) e^{-ik_z z - i\omega t} \phi_d(k_z,\omega)\, d\omega dk \tag{6}$$

where z is the depth increasing downward by convention, t represents the time, k_z is the depth wavenumber, ω denotes the angular frequency, and $\phi_d(k_z,\omega)$ is the cut-off filter symbolizing the first and third quadrant of the $f - k_z$ domain, given by:

$$\phi_d(k_z,\omega) = \begin{cases} 1 & \text{if } \omega k_z \geq 0 \\ 0, & \text{if } \omega k_z < 0. \end{cases} \tag{7}$$

Equations 6 and 7 take advantage of the causality principle implied in the wave equation, indicating that for a forward time propagation process, there must be increases in depth with increases in time in order to keep the phase constant. The up-going component of the source wavefield, $s_u(z,t)$, is obtained similarly by the 2D inverse Fourier transform after applying the corresponding cut-off filter:

$$\phi_u(k_z,\omega) = \begin{cases} 0 & \text{if } \omega k_z \geq 0 \\ 1, & \text{if } \omega k_z < 0. \end{cases} \tag{8}$$

It is worth mentioning that the decomposition needs to be done at each subsurface location where the evolution of the wavefield with time simulates a VSP data structure, as seen in Figure 3. For this reason, the spatial variables x and y have been suppressed from Equation 6. For a 3D wavefield, this process is repeated separately for each surface pair of coordinates $\vec{x} = (x,y)$ since the separation is implemented in $z - t$ seismic sections. In this report, I worked with 2D models where the wavefield propagation is represented as a 3D (x,z,t) space-time volume. Therefore, I only keep each horizontal coordinate x fixed every time the wavefield decomposition in the vertical direction is applied. Then I stack all the horizontal contributions to get the final separated components. Equations 6, 7, and 8 show how to decompose the source wavefield into up-going and down-going components in the $f - k_z$ domain, but the same process is valid for deblending the receiver wavefield. It is also possible to perform a horizontal decomposition replacing z by x in the previous equations.

Taking a generic 2D wavefield, $p(x,z,t)$, the algorithm for the vertical decomposition implemented in this report is described as follows:

For each horizontal coordinate x_i:

1. Select the corresponding $z - t$ seismic section, $p(x = x_i, z, t) = p(z, t)$.
2. Calculate the 2D Fast Fourier Trasnform (2DFFT) of $p(z, t)$, $\hat{P}(k_z, \omega)$.
3. Select the appropriate quadrants using the cut-off filters to separate the down-going events, $\hat{P}_{z+}(k_z, \omega)$, from the up-going events $\hat{P}_{z-}(k_z, \omega)$.
4. Apply the 2D Inverse Fourier Transform (2DIFFT) on $\hat{P}_{z+}(k_z, \omega)$ and $\hat{P}_{z-}(k_z, \omega)$ to get the decomposed components in the $z - t$ domain.

Filtering signal around the origin of the $f - k$ domain can be challenging because most of the energy is contained in this region. To avoid signal leaking artifacts, the original cut-off filters, ϕ_d and ϕ_u, are modified by leaving a gap of dimensions [-0.01, 0.01] m^{-1} in the wavenumber axis, and [-3, 3] Hz in the frequency axis (which is equivalent to applying a low-cut filter in both dimensions). These values were determined heuristically and kept constant throughout all the numerical simulations, regardless of the model dimensions. Additionally, each cut-off filter was convolved with a rectangular Gaussian taper to reduce truncation artifacts. Figure 4 shows the final form of the filters.

The main drawback of the previous workflow is the computation and memory requirements. The Fourier transform on the time dimension demands the storage of the wavefield snapshots at all the time-steps Δt. As the decomposition is done in both source and receiver wavefields, the algorithm stores two space-time volumes, which can be prohibitive depending on the model dimension and the total number of time-steps. On the other hand, most RTM schemes only store the source wavefield and apply the imaging condition “on the fly” while the receiver wavefield is backward propagated. To reduce the memory limitation, we can use a decimation strategy in which the snapshots are undersampled to approach the limit imposed by the Nyquist frequency:

$$f_{\mathrm{Ny}} = \frac{1}{2\Delta t}. \tag{9}$$

Therefore, each wavefield can be resampled at a larger time-step interval, Δt_{Ny}, as long as it complies with Equation 9. Figure 1 shows this procedure for a 2D model (i.e., a 3D space-time volume). In this study, I saved only every tenth frame to be correlated for imaging. This value optimizes the trade-off between the decimation process and the image quality, according to Youn and Zhou (2001). Finally, before applying the 2DFFT operator, the signal was zero-padded in depth and time dimensions to avoid wrap-around artifacts.[*]

NUMERICAL EXPERIMENTS

In this section, I present the RTM results obtained by applying the decomposed imaging condition algorithm on two 2D synthetic data sets, and I compare them with the conventional approach. The data sets are modeled with a 2D time-domain finite-difference propagator, employing an eight-order stencil in space, a second-order approximation in time, and a Ricker wavelet with a maximum frequency of 30 Hz as the seismic source function. Both models are discretized in a regular mesh with 5 meters gridpoint spacing. Absorbing

---

[*] The new size of the zero-padded sections was defined by calculating the nearest power of 2 sequence length in each dimension.

boundary conditions are used in the four boundaries of the discretized domain, including the top boundary. Consequently, there are no free-surface related multiples in the data sets. Additionally, I simulate a pre-processing step where the direct waves and the diving waves (which do not contribute to the imaging process) are removed from the shot gathers, using a smoothed version of the real velocity models (Schuster, 2017). The smoothed velocity models are also used as the background velocities for the migration algorithm.

Three-layer model

The first experiment tests the performance of the wavefield decomposition algorithm for a simple three-layer model. The model is shown in Figure 2 and has dimensions $N_z \times N_x = 81 \times 201$ points. The total recording time in the seismic data set is $\mathrm{T}_{\max} = 1$ second. As an example, the decomposition workflow is shown using a vertical $z-t$ section of the source wavefield for a receiver at $x = 300$ meters, displayed in Figure 3. This section shows a down-going wavefield with a strong amplitude, as well as two up-going reflections. Also, a secondary internal down-going event appears approximately at $t = 0.25$ seconds.

Figure 4 depicts the decomposition process in the $f-k$ domain: Figures 4.a and 4.b show, respectively, the amplitude spectrum of the vertical seismic section from Figure 3, without and with amplitude gains. Figures 4.c and 4.e presents the cut-off down-going and up-going mask filters, ϕ_d and ϕ_u; while Figures 4.d and 4.f show the amplitude spectrum after filtering. On the other hand, Figure 5 shows the separated components back in the $z-t$ domain after applying the 2DIFFT, where the vertical decomposition is effectively accomplished. However, the up-going source wavefield has artifacts caused by leaking of wavefields propagating laterally, which are not considered in the vertical decomposition strategy. Figure 6 displays a snapshot at $t = 0.3$ seconds of the total reconstructed wavefields, in which the lateral artifacts are more notorious.

After applying the same procedure to the receiver wavefield, a single shot RTM is performed separately on each individual pair of the imaging condition in Equation 4 (Figure 7). From this result, it can bee seen that most of the backscattered low-frequency signal is caused by the cross-correlation of the acausal pairs, $s_u r_u$ (Figure 7.b) and $s_d r_d$ (Figure 7.c). This noise is mostly manifested near the critical angle. Conversely, the characteristic eliptic-shaped migration kernel is present in the causal crosscorrelation given by $s_d r_u$, which corresponds to the high wavenumber part of the reflectivity image. Although the product between the other causal pair, $s_u r_d$, contains some artifacts, it also has information about the reflector positions, as can be seen near the first reflector at $z = 150$ meters. Finally, Figure 8 compares the RTM results obtained by implementing the conventional imaging condition and the decomposed imaging condition. The latter significantly reduces the backscattering noise in the image.

Sigsbee2a model

The second experiment presents a more realistic scenario and tests the decomposed imaging condition in a small portion of the Sigsbee2a model (Paffenholz et al., 2002). This model has dimensions of $N_z \times N_x = 201 \times 351$ points and the total recording time is $\mathrm{T}_{\max} = 1.5$ seconds. The imaging of the Sigsbee2a model is more challenging than the previous model because of the complexity of the geological structure, a varying water-bottom reflectivity, and a syncline structure delimited by the sharp top of a high-velocity salt body. In this case, a full 2D acquisition with 55 shots is simulated. Figures 9, 10, and 11 show the real velocity model, the background velocity model, and the reflectivity model, respectively.

The conventional RTM result of the entire 2D line is shown in Figure 12. As expected, the backscattered noise caused by the presence of the salt body entirely mask all the reflectors. A high-pass Laplacian filter is applied to the migration image as a post-imaging technique to remove the low-frequency artifacts (Figure 13). Although the high-pass operator effectively suppresses most of the backscattered signal, imaging artifacts appear at the irregular top salt boundary due to the strong scattering effect. Besides, low-wavenumber residuals and strong high-dip artifacts remain, especially in the areas close to the salt body. When the decomposed imaging condition is applied (Figure 14), we see that it does not produce the backscattered noise, providing sharper reflectors overall and especially around the syncline structure. Also, the low-wavenumber components of the acquisition footprint near the surface have been partially removed, which facilitates the interpretation of shallow reflectors.

CONCLUSIONS

The use of the two-way wave equation in RTM is a double-edged sword. On the one hand, it enables the imaging of complex structures without dip or lateral velocity limitations. On the other hand, it generates backscattering noise that contaminates the reflectivity image and hinders the interpretation of shallow and deep reflectors. Using a wavefield decomposition technique in the $f - k_z$ domain, it was demonstrated the effectiveness of the decomposed imaging condition for removing the backscattered noise in RTM images. From the three-layer model experiment, it can be concluded that wavefields propagating in lateral directions (i.e., left-going and right-going waves) also need to be attenuated to avoid high-amplitude artifacts that leak into the separated components. Although effective, the wavefield decomposition technique presented in this report can be prohibitively expensive, especially for 3D models. A decimation strategy in the wavefield storage partially reduces the memory limitations, but further studies need to be develop towards minimizing the computational requirements of this and others wavefield decomposition techniques, considering the advantages they offer in comparison to the conventional imaging approach.

REFERENCES

Baysal, E., D. D. Kosloff, and J. W. C. Sherwood, 1983, Reverse time migration: Geophysics, **48**, 1514–1524.

Claerbout, J. F., 1985, Imaging the earth's interior: Blackwell Scientific Publications, Ltd.

Díaz, E., and P. Sava, 2012, Understanding the reverse time migration backscattering: Noise or signal?: Society of Exploration Geophysicists International Exposition and 82nd Annual Meeting 2012, SEG 2012, 3380–3385.

Etgen, J., S. H. Gray, and Y. Zhang, 2009, An overview of depth imaging in exploration geophysics: Geophysics, **74**, WCA5–WCA17.

Fletcher, R. P., P. J. Fowler, P. Kitchenside, and U. Albertin, 2006, Suppressing unwanted internal reflections in prestack reverse-time migration: GEOPHYSICS, **71**, E79–E82.

Guitton, A., B. Kaelin, and B. Biondi, 2007, Least-squares attenuation of reverse-time-migration artifacts: GEOPHYSICS, **72**, S19–S23.

Hu, L. Z., and G. A. McMechan, 1987, Wave-field transformations of vertical seismic profiles.: Geophysics, **52**, 307–321.

Jin, H., G. A. McMechan, and H. Guan, 2014, Comparison of methods for extracting adcigs from rtm: GEOPHYSICS, **79**, S89–S103.

Jing, C., and J. E. Anderson, 2019, *in* Dip-guided Laplacian image filter for RTM: 4131–4135.

Leveille, J. P., I. F. Jones, Z.-z. Zhou, B. Wang, and F. Liu, 2011, Subsalt imaging for exploration, production, and development: A review: Geophysics, **76**, WB3–WB20.

Liu, F., G. Zhang, S. A. Morton, and J. P. Leveille, 2011, An effective imaging condition for reverse-time migration using wavefield decomposition: Geophysics, **76**.

Paffenholz, J., B. McLain, J. Zaske, and P. J. Keliher, 2002, Subsalt multiple attenuation and imaging: Observations from the Sigsbee2B synthetic dataset: SEG Technical Program Expanded Abstracts 2002, Society of Exploration Geophysicists, 2122–2125.

Paniagua-Castrillón, J. G., and O. L. Quintero-Montoya, 2018, Application of the continuous wavelet transform in the extraction of directional data on RTM imaging condition wavefields: CTyF - Ciencia, Tecnologia y Futuro, **8**, 65–73.

Schuster, G., 2017, Seismic inversion: SEG.

Wang, F., H. Chauris, D. Donno, and H. Calandra, 2013, Taking advantage of wave field decomposition in full waveform inversion: 75th European Association of Geoscientists and Engineers Conference and Exhibition 2013 Incorporating SPE EUROPEC 2013: Changing Frontiers, 135–139.

Wang, F., D. Donno, H. Chauris, H. Calandra, and F. Audebert, 2016, Waveform inversion based on wavefield decomposition: Geophysics, **81**, R457–R470.

Whitmore, N. D., 1983, *in* Iterative depth migration by backward time propagation: 382–385.

Yoon, K., and K. J. Marfurt, 2006, Reverse-time migration using the poynting vector: Exploration Geophysics, **37**, 102–107.

Youn, O., and H.-w. Zhou, 2001, Depth imaging with multiples: Geophysics, **66**, 246–255.

Zhang, Y., and J. Sun, 2009, *in* Practical issues of reverse time migration: True amplitude gathers, noise removal and harmonic-source encoding: 204–204.

FIGURES

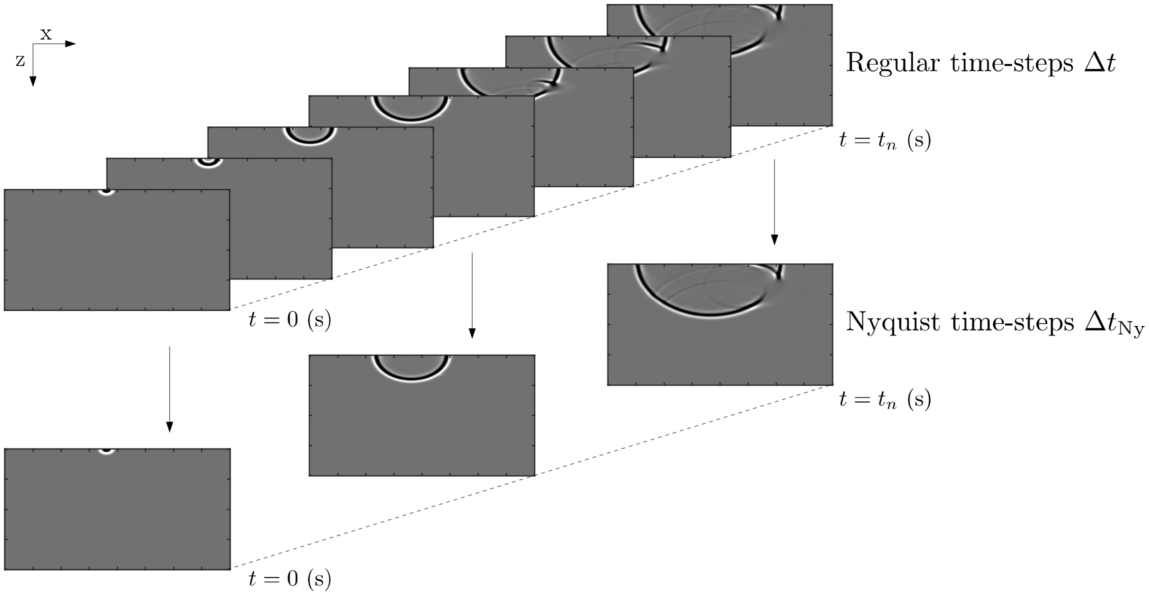

Figure 1: An illustration of the decimation strategy. All the snapshots of the wavefield (above) are undersampled to reduce memory usage (below).

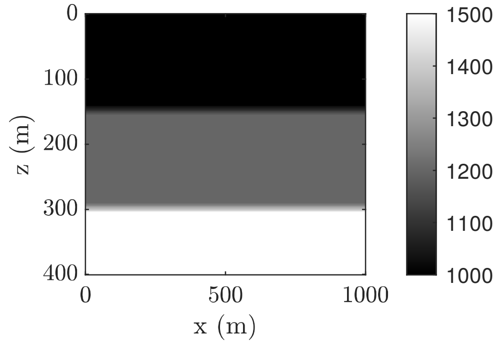

Figure 2: The three-layer velocity model.

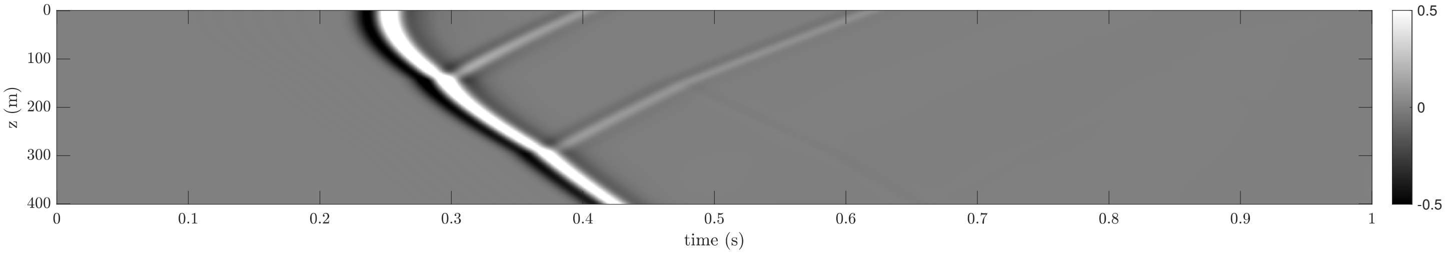

Figure 3: Source wavefield $z{-}t$ section recorded at $x = 300$ meters. The source is propagated from the surface at $x = 500$ meters. The data structure resembles a VSP section.

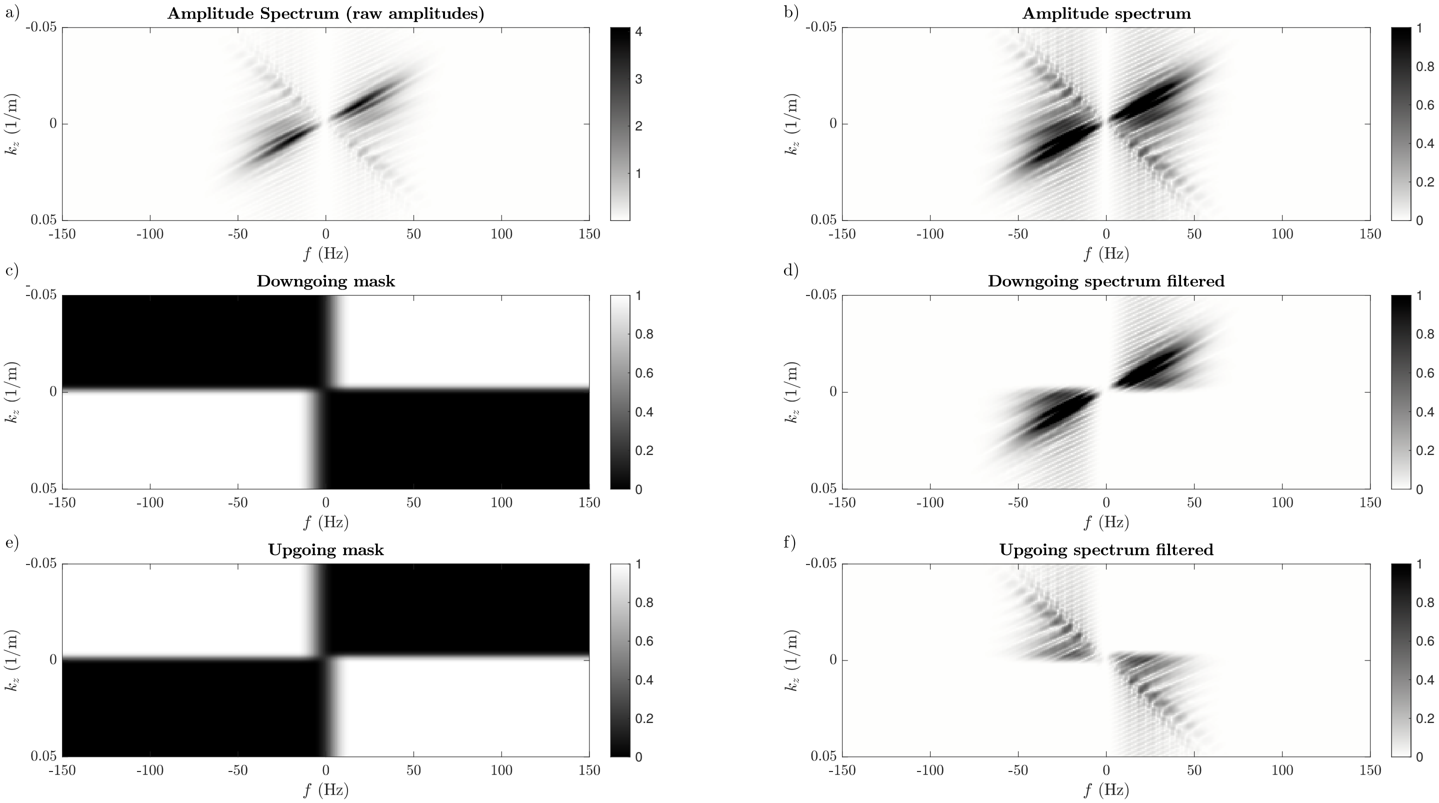

Figure 4: Deblending of the source wavefield section from Figure 3 in the $f-k$ domain.

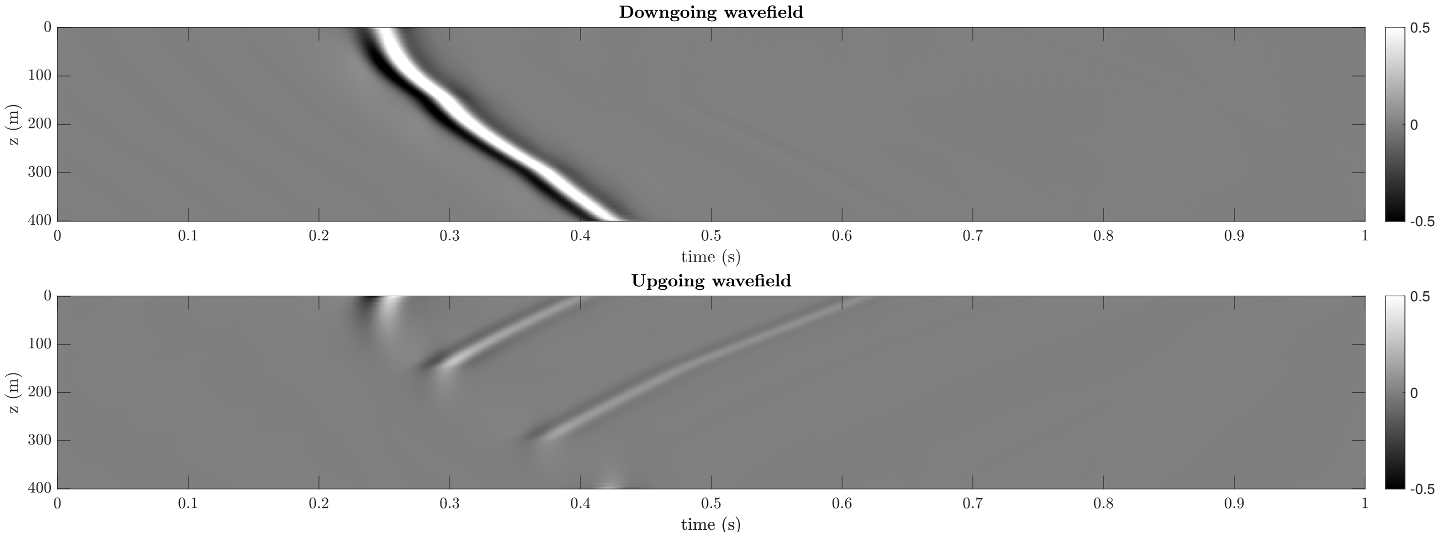

Figure 5: Decomposed source wavefield components, s_d (above) and s_u (below), in the $z-t$ domain.

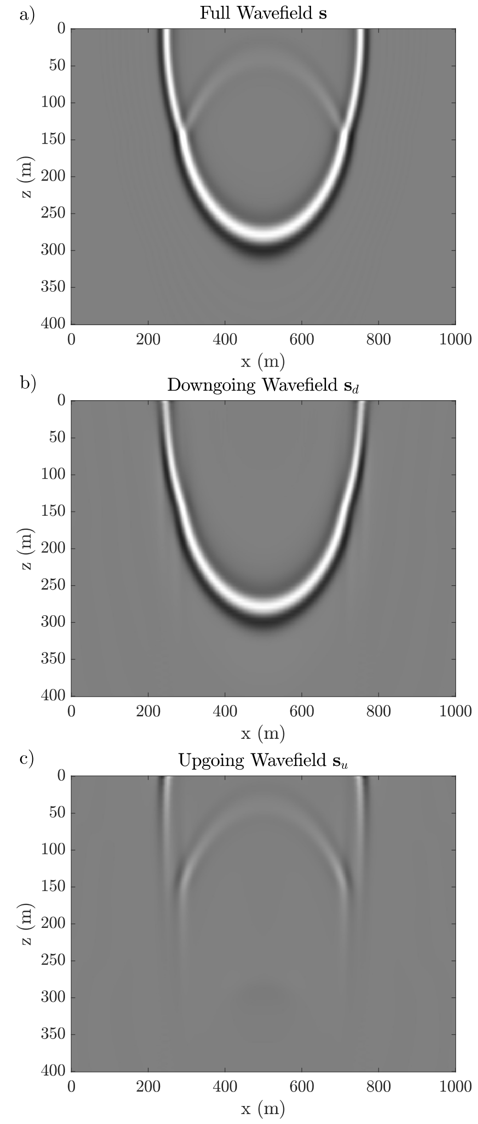

Figure 6: Source wavefield decomposition at t=0.3 seconds. The initial source wavefield is displayed at the top for comparison. Note the strong lateral waves leaked in the up-going component, s_u.

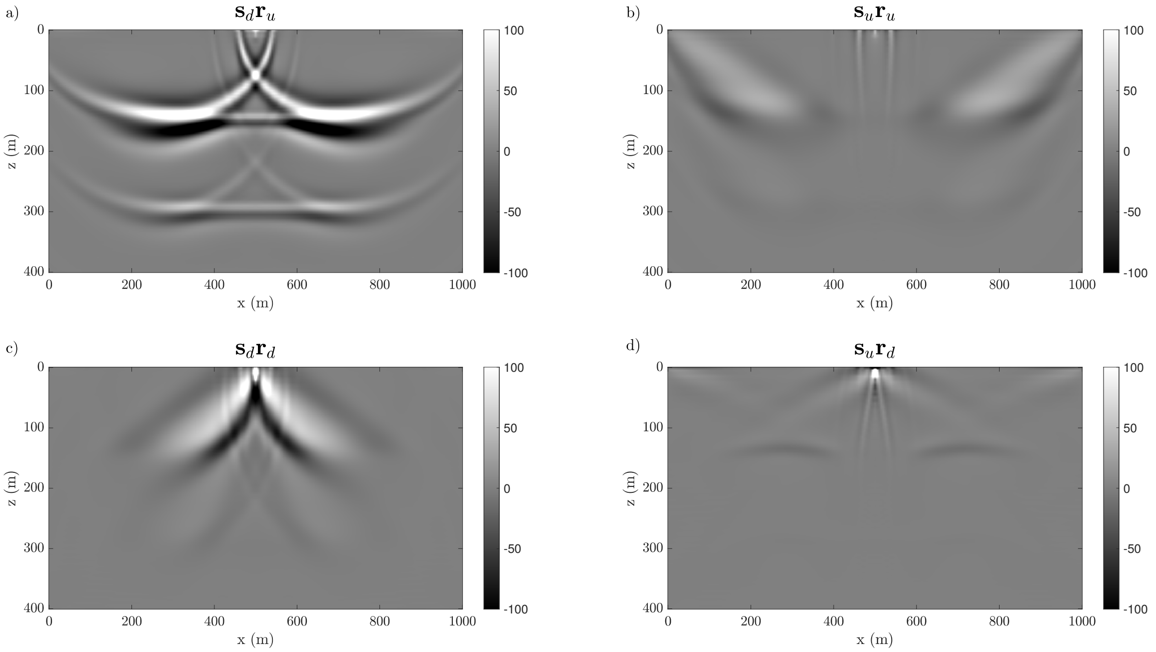

Figure 7: RTM results from the individual cross-correlations of each wavefield pair in Equation 4. a) Cross-correlation between the down-going component of the source wavefield and the up-going component of the receiver wavefield (causal pair). b) Cross-correlation between the up-going components of both the source and receiver wavefields (acausal pair). c) Cross-correlation between the down-going components of both the source and receiver wavefields (acausal pair). d) Cross-correlation between the up-going component of the source wavefield and the down-going component of the receiver wavefield (causal pair).

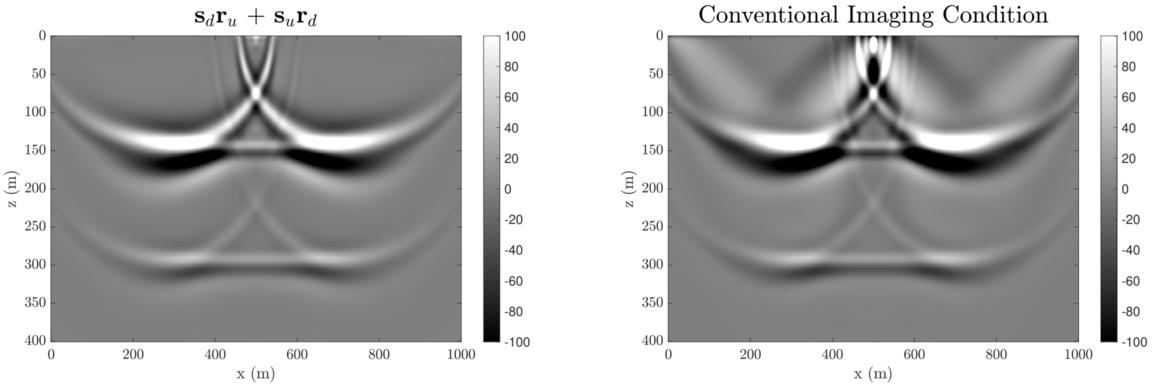

Figure 8: Single shot RTM results using the decomposed imaging condition (left) and the conventional imaging condition (right).

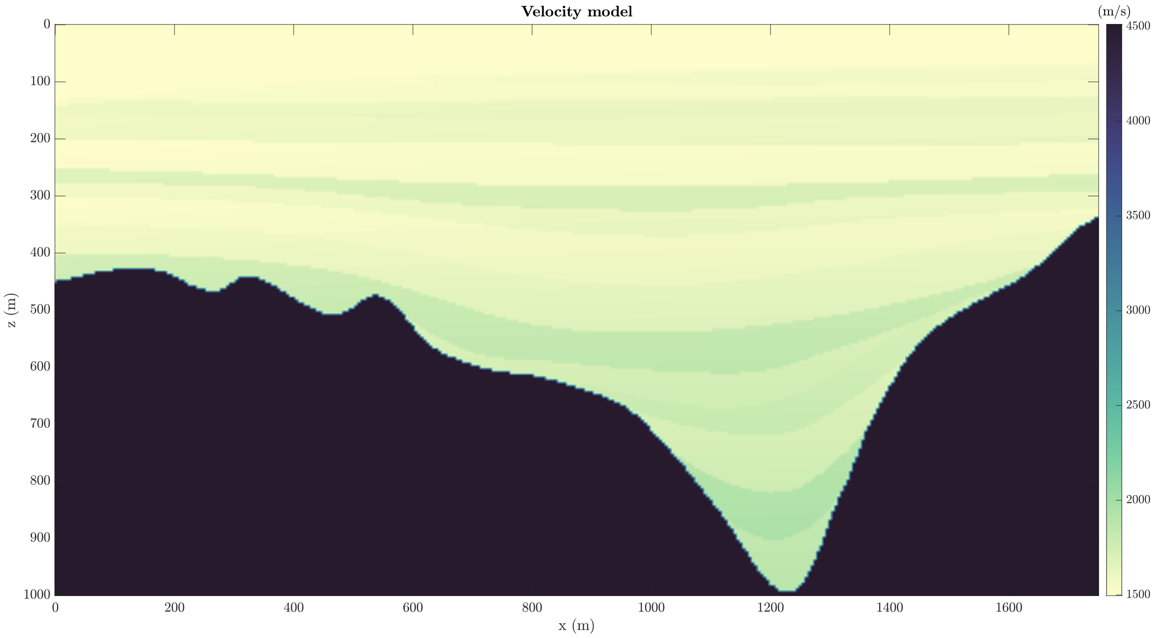

Figure 9: Velocity of the modified Sigsbee2a model.

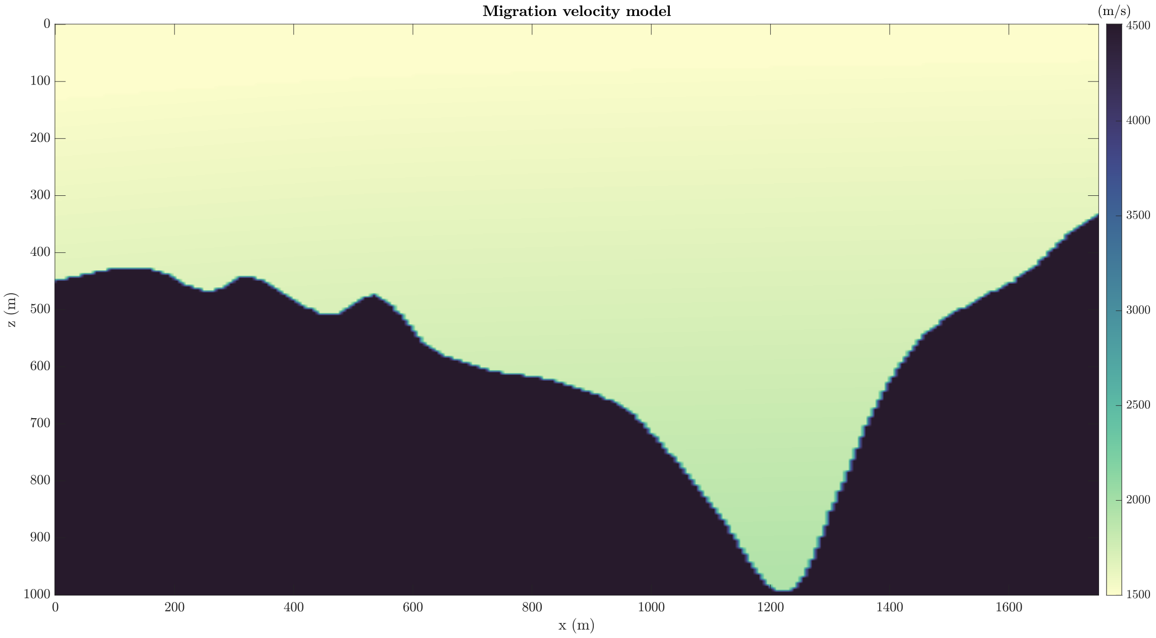

Figure 10: Background velocity model used for RTM imaging.

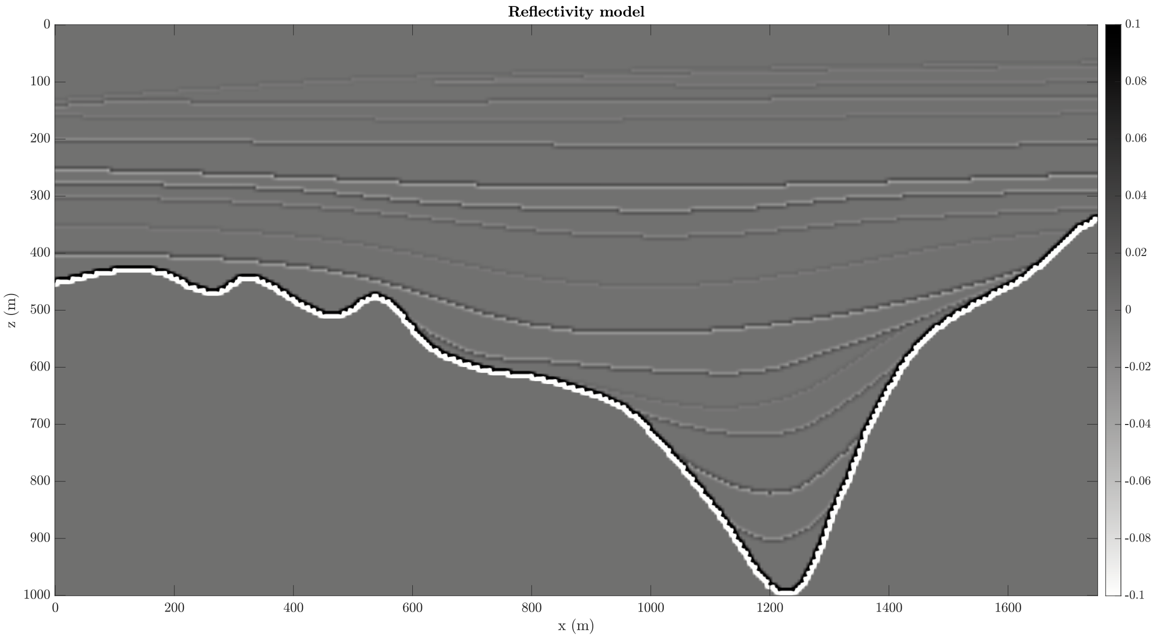

Figure 11: Reflectivity of the modified Sigsbee2a model.

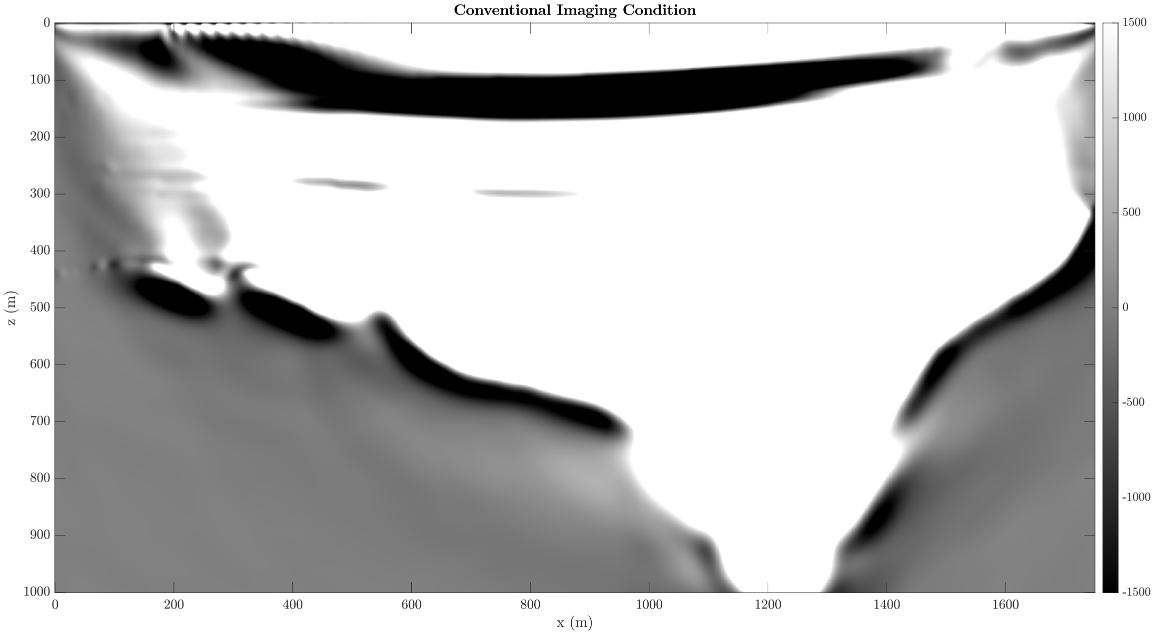

Figure 12: The RTM result using the conventional cross-correlation imaging condition.

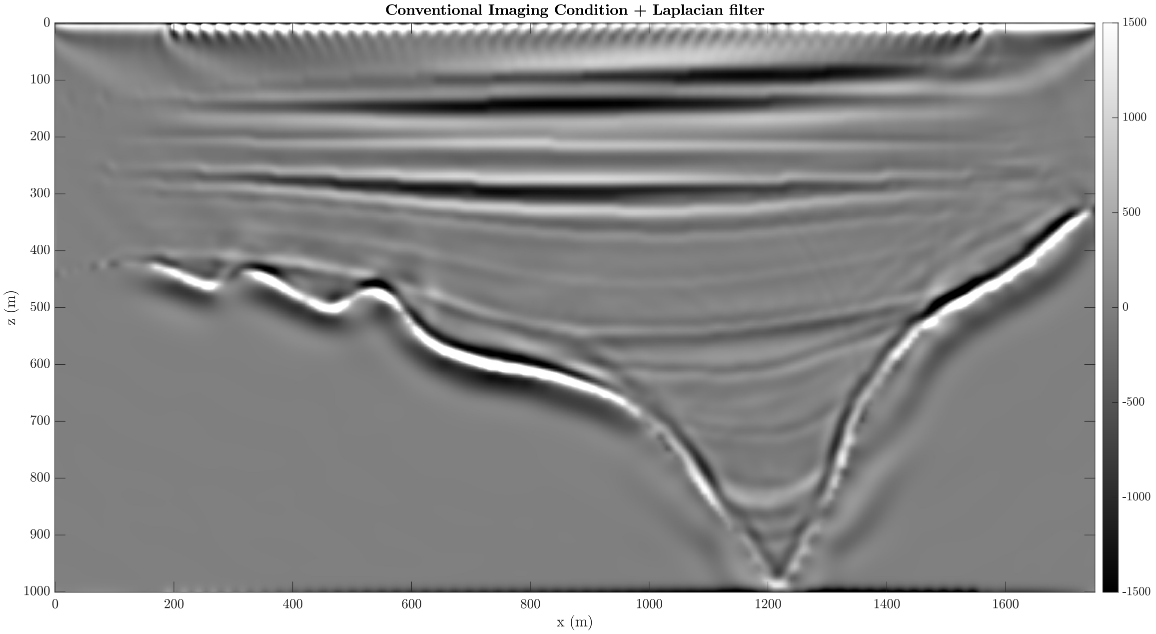

Figure 13: Band-pass filtered result of the image in Figure 12.

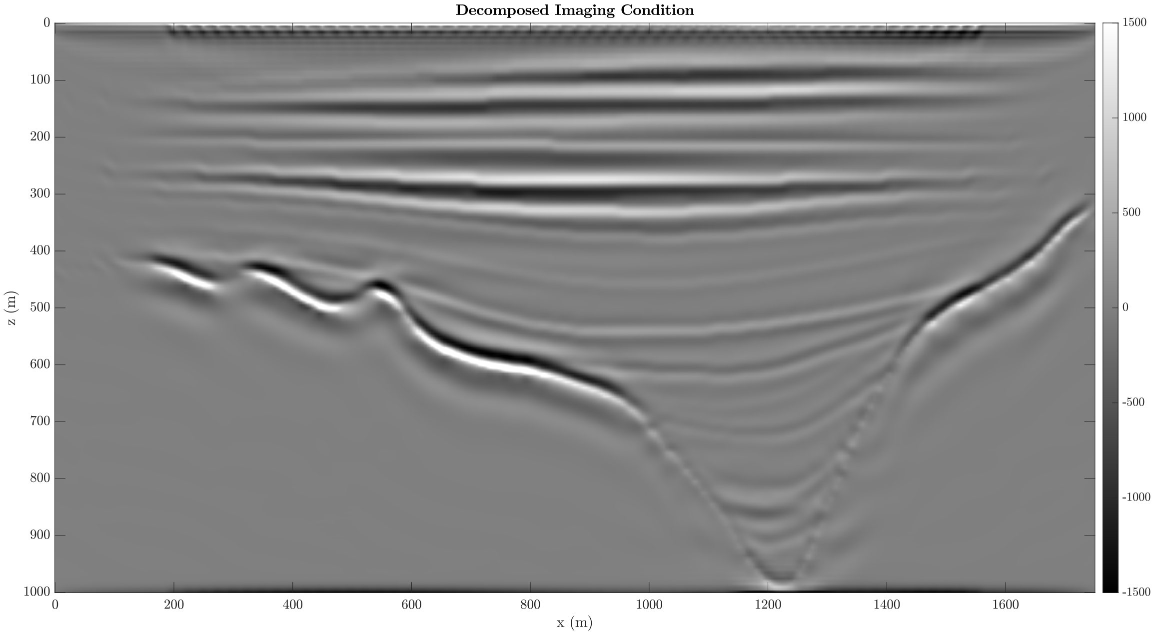

Figure 14: The RTM image using the decomposed imaging condition. No artifacts around the large contrast salt interface is observed.